Planetary and Space Science 265 (2025) 106153

Contents lists available at ScienceDirect

Planetary and Space Science

journal homepage: www.elsevier.com/locate/pss

Seismic wave experiments in granular media with applications to asteroids

Thomas Gallot *, Camila Sedofeito, Alejandro Ginares, Gonzalo Tancredi

Instituto de Física, Facultad de Ciencias, Universidad de la República, Montevideo, Uruguay

ARTICLE INFO

Dataset link: http://www.k-wave.org/

Keywords:
Granular media
Seismic waves
Nonlinear elasticity
Asteroids
Planetary structure
Microgravity
Regolith

ABSTRACT

Observational data support the view of asteroids as granular systems. Characterizing their mechanical properties is crucial for space mission planning, assessing Earth's impact risks, and understanding solar system origins. In this context, we present a laboratory-scale experiment aimed at examining wave propagation in granular media. Our findings demonstrate that the propagation of observed waves at 500 Hz shows significant attenuation with an estimated value of $\alpha = (1.8 \pm 0.2)$ Np/m. Additionally, we observe an increase in wave speed with confining pressure, which follows a dependency on $p^{1/2}$, interpreted as mesoscopic nonlinear elasticity. This indicates that a confined granular medium behaves as a nonlinear consolidated medium. Furthermore, we establish the equivalence of propagation properties between impact and vibration by supporting our experimental data analysis with numerical simulations. Applying our findings to model wave propagation in a low-gravity setting involving Dimorphos' mass and geometry, our laboratory-based approach offers a cost-effective alternative to in situ measurements.

1. Introduction

Granular materials serve as valuable laboratory-scale systems for studying complex natural phenomena. They are crucial to comprehending the dynamics of the Earth's surface and seismic activity (Rubinstein et al., 2007; Latour et al., 2013; Aichele et al., 2020). Moreover, granular materials play a crucial role in unravelling the properties and behavior of planetary surfaces, including notable examples such as the sand dunes on Mars, the regolith on the Moon, and the surfaces of asteroids.

Currently, there is a wealth of observational evidence corroborating the idea that asteroids are composed of aggregations of rocks, resembling the rubble-pile structure observed in the case of Itokawa by the Hayabusa mission (Fujiwara et al., 2006). Several other space missions exploring diverse asteroids have confirmed the prevalence of this rubble-pile structure: Hayabusa 1 and 2 visited Itokawa (Fujiwara et al., 2006) and Ryugu (Watanabe et al., 2019), Osirix-Rex visited Bennu (Lauretta et al., 2019), and DART visited Didymos and Dimorphos (Daly et al., 2023). In addition, numerous indirect pieces of evidence supporting the structure of the rubble pile have also been systematically reviewed by Scheeres et al. (2015) and Walsh (2018).

This work is therefore motivated by the need for experimental data to understand how granular-like asteroids respond to impacts. This understanding is significant for assessing the collision hazard posed by asteroids to Earth and for advancing exploration efforts related to asteroids (Hestroffer et al., 2019). Furthermore, it contributes to a broader understanding of the collisional processes integral to the formation and evolution of our solar system (Holsapple, 1993). Specifically, our interest extends to unraveling the nature of the so-called active asteroids, as coined by Jewitt (2012); These are asteroids exhibiting a temporary tail, potentially generated by a shaken mechanism induced by the propagation of a mechanical perturbation far from the impact point (Tancredi, 2015; Tancredi et al., 2023; Raducan et al., 2024).

A potential alternative for deflecting an asteroid on a collision course with Earth is the kinetic impact method, which involves striking the asteroid with an object of significant mass and high velocity to transfer linear momentum and alter its trajectory. NASA launched the DART mission to assess this technology (Rivkin et al., 2021); the experiment was conducted successfully on September 26, 2022 (Daly et al., 2023). The success of the deflection strategy depends on several elements, such as the occurrence of craters (Stickle et al., 2022), the spread of momentum throughout the ejecta (Fahnestock et al., 2022; Li et al., 2023) and the energy transmission to the interior through seismic waves and deformation processes (Tancredi et al., 2023; Raducan et al., 2024). An energy and momentum budget of the DART experiment is still missing, accounting for the contribution of the above sources to the transfer of energy and momentum.

The images released at the time of impact showed that the target, the 160 m asteroid Dimorphos, resembles a rubble pile that exhibits surface boulders of various sizes, some as small as a few centimetres (Barnouin et al., 2024; Pajola et al., 0000). With the NASA-DART

---

* Corresponding author.
E-mail address: tgallot@fcien.edu.uy (T. Gallot).

https://doi.org/10.1016/j.pss.2025.106153
Received 22 November 2024; Received in revised form 12 June 2025; Accepted 15 June 2025

mission, impacting an asteroid to deflect its trajectory is no longer science fiction. Dimorphos was successfully deflected (Thomas et al., 2023; Cheng et al., 2023), and the contribution of the ejected material to the linear momentum budget was found to be significant (Li et al., 2023). The impact induced a significant ejection of material, observed in seconds at a wide range of ejection velocities. The presence of a tail, sustained for several months due to Solar Radiation Pressure, indicates that materials are escaping at very low velocities (Li et al., 2023; Moreno et al., 2023). This underscores that direct impact is not the only factor that contributes to ejection. Seismic waves propagating throughout the asteroid from the impact site also play a role in material expulsion, adding to the overall contribution to the linear momentum budget (Li et al., 2023; Moreno et al., 2023). However, preliminary results on the effect of particles ejected in the antipodal hemisphere showed that the contribution to angular momentum transfer would be negligible (Tancredi et al., 2023). A result that should be revised with detailed simulations and the analysis of the observed ejected material.

Hence, it is crucial to investigate the propagation of seismic waves induced by impacts on granular materials to better understand the consequences of a NASA-DART-like experiment. Seismic activity on asteroids plays a key role in their surface evolution, internal structure, and response to external forces. Seismic shaking from micrometeoroid impacts can induce regolith movement, as shown by Garcia et al. (2015). The role of seismic reverberation in shaping asteroid morphology was explored by Quillen et al. (2019), who identified antipodal focusing and normal mode excitation, while Sánchez et al. (2022) demonstrated that energy dissipation in granular asteroid interiors is extremely high. Tidal forces can also generate seismic activity, as simulated for Apophis (DeMartini et al., 2019) and binary asteroids (DellaGiustina et al., 2024; Ballouz et al., 2014). Murdoch et al. (2017) investigated impact dynamics in low gravity, revealing differences in penetration and energy dissipation compared to Earth. These studies highlight the importance of seismic analysis for understanding asteroid interiors, regolith dynamics, and planetary defense strategies.

Several experimental studies have investigated wave propagation in granular media under impact, considering both unconfined conditions (Yasui et al., 2015) and confined scenarios (van den Wildenberg et al., 2013; Martínez et al., 2021). In weakly confined granular media, van den Wildenberg et al. (2013) observed that shock waves, when present, remain largely unaffected by confining pressure. However, at confining pressures comparable to those in our experiments, no shock wave was detected; instead, a quasi-linear sound wave was observed, whose speed does depend on confining pressure. Beyond impact-generated waves, recent studies have explored wave velocity variations at low confining stresses, which are particularly relevant for planetary surface materials. Experiments on Martian regolith simulants have demonstrated that compression and shear wave velocities follow a power law dependency on stress, though deviations from purely elastic behavior are observed (Betancourt et al., 2023). Theoretical models incorporating granular contact mechanics and asperity effects provide good agreement with experimental results at high pressures (Caicedo et al., 2023).

The confining pressure stands out as a crucial parameter governing the properties of the material, with strongly compressed granular media exhibiting solid-like characteristics, while lightly compressed media exhibit a highly variable mechanical response (Gómez et al., 2012). The microgravity conditions prevalent on asteroids confer unique mechanical properties on granular media that are difficult to replicate on Earth (e.g. Altshuler et al., 2014; Villalobos et al., 2022).

Despite these challenges, experiments under such conditions play a fundamental role in validating numerical models, particularly Discret Element Method (DEM) (e.g. Schöpfer et al., 2009; Wang and Mora, 2009; Tancredi et al., 2012), that address the intricate physics of granular mechanics (Duran, 2012). The ESA Hera mission will observe and characterize the asteroid Dimorphos to study the effects of the DART impact, as described in Michel et al. (2022). The results from this mission will be a unique opportunity to link numerical simulations of impacts into granular media and large-scale impact experiments.

In this study, we propose an experimental work of laboratory-scaled asteroid impacts. An important distinction between experiment on Earth and real asteroids is the gravity conditions. The stress distribution induced by self-gravity within an asteroid is not well known, and estimates vary (see different estimates by: Cheng, 2004; Sharma, 2013; Zhang et al., 2018). However, it is acknowledged that a pressure gradient exists with increasing values toward the interior of the body, dependent on the compaction states of the granular media during asteroid formation and ulterior long-term evolution. In this experiment, we propose to characterize the wave propagation at different confining pressures of a granular medium to understand the effect of the pressure gradient. Additionally, we address the equivalence between wave propagation resulting from impacts and those induced by a shaker. This equivalence is of interest for conducting non-impact testing to assess the properties of granular materials in low-gravity conditions.

The response to mechanical excitation in granular media exhibits a coherent wavefront, as observed in studies such as Somfai et al. (2005). Effective Medium Theory (EMT) (Walton, 1987), predicts the scaling of P-wave speeds with pressure. This scaling follows $p^{1/6}$ for Hertzian contacts or $p^{1/3}$ when considering non-Hertzian contacts or variations in the coordination number C (Goddard, 1990). Observations from both DEM and experimental studies underscore the lack of consensus in the literature on this scaling, as detailed in (see Jia et al., 2021 for a non-exhaustive review). The same work also points out a deficiency in experimental estimates of elastic wave attenuation in granular media.

This investigation helps to predict the consequences of impacts on asteroids, including the generation of regoliths and alterations in surface morphology. A better understanding of wave propagation in granular materials is essential for interpreting potential seismic measurements on asteroids. If such measurements were conducted, seismological analysis could provide insights into subsurface properties, including the presence of volatiles such as water ice. See Murdoch et al. (2017) for seismological approaches applicable to Dimorphos. Furthermore, it contributes to our understanding of how asteroid surfaces respond to internal or external forces, thus helping to interpret events such as landslides or internal movements (Watters et al., 2011; Housen and Wilkening, 1982).

In Section 2, we detail the experimental setup and outline the primary hypothesis guiding our methodology. The experiments were carried out within a cubic container filled with various granular materials under confining pressure. This pressure emulates the stress conditions that increase with depth and scale within the interior of a rubble-pile asteroid. The experimental observations and the characterization of wave propagation are detailed in Section 3.1. In Section 3.2, a viscoelastic numerical simulation analysis ensures that the observed wave properties are not biased by the diffraction effects of the experimental configuration. In Section 4, we discuss the implications of the dependence of wave speed on the confining pressure and the nature of the granular material. We further extrapolate our findings to numerically simulate wave propagation in a low-gravity asteroid comparable to Dimorphos. The overarching findings and implications derived from these observations are elucidated in the concluding remarks in Section 5.

2. Experimental setup

The granular medium is confined within a cubic box with a side length of $L = 50$ cm, representing the internal distance between the lateral walls (see Fig. 1). The coordinate system ($\vec{x}$, $\vec{y}$, $\vec{z}$) is centred at the impact point, as illustrated in Fig. 1. The walls are constructed from 14-mm thick transparent acrylic. The cube features a sliding top lid and is positioned on a movable platform. In order to facilitate the direct impact of the projectile or to allow contact of the shaker with the material, a circular aperture with a diameter of 16 cm is included. The internal top lid remains immobile, being firmly welded to the hydraulic

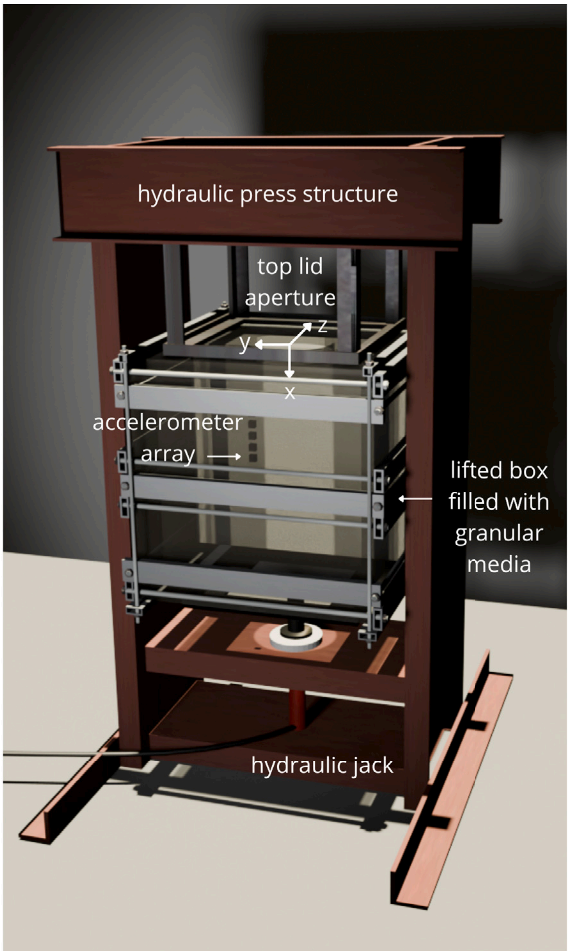

Fig. 1. A cubic acrylic box with a side length of 50 cm, filled with granular material, is set on a moving platform. The granular media is contained within the box, lifted by a hydraulic jack while the top cover, welded on the structure, stays static. The aperture in the top lid facilitates direct interaction between the granular media and the projectile or shaker. Seismic waves during loading-unloading cycles are recorded by a vertical array of accelerometers immersed in the media.

press structure. The upward movement of the box is facilitated by a hydraulic jack (Enerpac RC106 with a 15-cm stroke), which compresses the material. The hydraulic press, designed for a maximum load of 10 tonnes, measures the internal cylinder pressure p_c using a pressure transmitter (Wika A-10). The hydraulic force F is then calculated as $F = p_c A_c$, with A_c representing the effective area of the hydraulic jack cylinder (manufacturer data: 14.5 cm^2).

The experiments involved three different granular materials: spherical glass beads, sand with a quartz-feldspathic composition, and gravel predominantly composed of granite clasts. Table 1 provides an overview of the key characteristics of each medium. The selection of these materials was made to discern potential influences stemming from size, material composition, and angularity. Scaling the experiment with an approximate 300-fold factor results in a Dimorphos-sized asteroid, with particle sizes ranging from 5 to 50 cm, overlapping with the lower range of boulders observed on the surface of Dimorphos (larger than 16 cm) (Daly et al., 2023; Pajola et al., 0000).

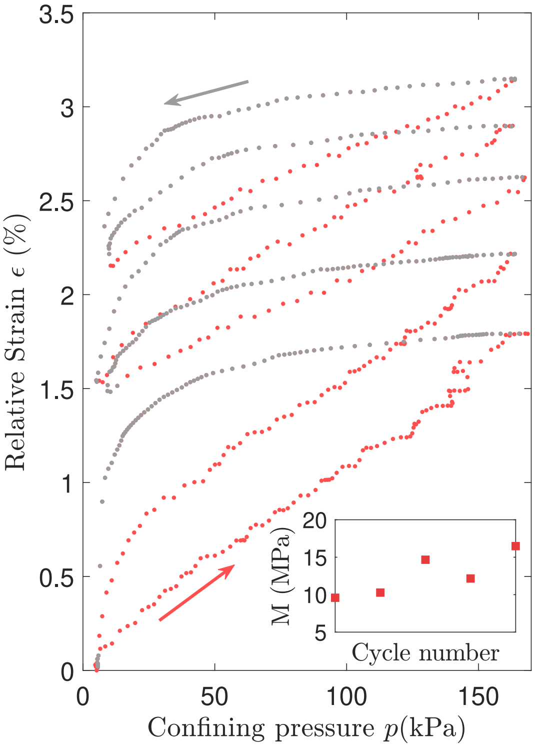

Fig. 2. Evolution of the strain ϵ as a function of the confining pressure p during five oedometric cycles in glass beads. The inverse of the slope during compression is the elastic modulus M and is represented as red squares in the inset. After five cycles of compression-relaxation, the final strain is 3% corresponding to a 15 mm displacement of the box or 600 times the grains diameter.

Table 1
The characteristics of the granular media employed in the experiments are as follows: (1) Glass beads characterized by zero angularity and a high spherical shape ratio. (2) Sand grains with angular to sub-angular features and a medium sphericity shape ratio. (3) Gravel grains exhibiting angularity and very low sphericity. The diameter corresponds to the mode of the size distribution determined by sieve analysis following the DIN 66165-2 standard. The initial volume fraction, in the absence of confining pressure, is measured through water saturation, as outlined in the experimental methodology (Badillo, 1974, Appendix III-c).

Material	Diameter d (μm)	Grain size (Wentworth scale)	Density ρ (g/ml)	Vol. fraction ϕ
Glass beads	250	Fine to medium sand	1.63	0.66
Sand	750	Coarse sand	1.66	0.64
Gravel	1500	Medium to coarse gravel	1.66	0.63

The granular material, stored in a 150-liter barrel, is lifted over the hydraulic press structure using an electric winch. Upon releasing the plug at the bottom of the barrel, the material flows into the box through its upper aperture. The barrel, deliberately weighted to provide a mass of $m = 195 \pm 1$ kg of grains, is emptied, and the resulting pile is manually leveled. Following the filling process, a series of five compression-relaxation cycles, spanning from unload to 200 kPa, is carried out to rearrange the grains on the surface of the pile.

The displacement of the box is monitored using a Pixelink PL-D722 digital camera with a one-second time lapse. A 1-D analysis is conducted on vectors created by averaging pixel values along a specific direction. The correlation between the initial image and subsequent frames is computed and the position of the maximum of the correlation provides estimates of displacements, u_x and u_y, along both directions, with an uncertainty of $\Delta_u = 50\,\mu\text{m}$. This uncertainty corresponds to the maximum displacement measured without moving the box. During peak loading, near the lateral walls, the lateral displacement is estimated as $u_y = 0 \pm \Delta_u$. The uncertainty, which is 0.01 % of the box size, can be considered negligible. This holds symmetrically for the displacement along the z-direction. In addition, the upper and lower walls are reinforced with steel structures, making them less deformable than the side walls. The only conceivable strain is along the x-direction where the strain is $\epsilon = u_x/L$ is induced by u_x, which represents the sinking of the top lid into the box.

The absence of wall deformation guarantees the even distribution of the force $\vec{F} = -F\vec{x}$ applied at the bottom of the box over the contact area $s = 0.25\ \mathrm{m}^2$ with the grains. The confining pressure, denoted as $p = F/s$, is a pivotal parameter in these experiments. It is a macroscopic stress uniformly applied along the x-direction at the bottom of the medium and reciprocated at the top surface of the granular medium. It is different from the volumetric pressure, which is proportional to the trace of the stress tensor.

Fig. 2 represents ϵ as a function of p. Five compression-relaxation cycles were recorded. The minimum pressure $p_{min} = 7.6$ kPa corresponds to the weight of the material distributed on the floor of the box when the hydraulic jack does not apply additional pressure. Then we increase the confining pressure by slowly pumping the hydraulic jack. The maximum pressure is manually set at $p_{max} = 164 \pm 5$ kPa during a controlled rising time, which varies between 10 and 150 s. No significant effect on strain measurements was observed within this time range. To picture hysteresis, the pale red dots correspond to the compression phase; while the gray dots correspond to the relaxation phase. After each compression-relaxation cycle, the strain does not return to zero. After five cycles, the maximum total strain is $\epsilon_{max} \sim 3\%$. This volume variation of the granular medium can be explained by three different phenomena: a reduction in mass, grain deformation, and compaction of the granular media.

We observe a small amount of material leaking through the edges of the sliding top lid. No damage to the glass beads has been observed by visual examination. If the maximum strain ϵ_{max} corresponds to a material leak, a mass variation $\Delta_m = m\epsilon_{max} \approx 5$ kg should be observed. Instead, the grains collected outside the box after a few cycles weigh less than 10 g, corresponding to a strain of approximately 10^{-5}. Since this value is two orders of magnitude smaller than the strain uncertainty, its effect is negligible, and the leakage can be ignored. Furthermore, under the hypothesis of a homogeneous distribution of stress over a layer of grains, the total strain for a classical sphere-sphere Hertzian contact (Dintwa et al., 2008) is $\epsilon = \left(3\sqrt{2}(1-\nu^2)p/E\right)^{1/3}$. With typical glass properties of Young's modulus $E = 70$ GPa and Poisson's ratio $\nu = 0.2$, this results in a strain of 0.04%, which is two orders of magnitude less than the measured strain. Therefore, we conclude that the main origin of the strain is a new compaction state of the granular medium due to material reorganization.

Seismic waves were generated at $x = y = z = 0$ through the aperture in the upper lid (see Fig. 1). Three distinct projectiles and a shaker in contact with the medium served as the sources. The acceleration of spherical projectiles was achieved using three devices: a spring-piston air rifle, a CO_2 pistol, and a crossbow. These devices were securely clamped to ensure that the shots were directed precisely to the same location and at a 90-degree angle. Detailed information on projectiles is provided in Table 2. An alternative seismic source used was a 10-kg portable shaker (APS-300), positioned on top of the granular medium. This device converts electrical signals into mechanical vibrations, producing controlled oscillations that propagate through the medium to generate seismic waves. The input signal was a Heaviside step function sent from a function generator (Rigol DG4062) to mimic a small impact.

Impacts or vibrations are induced along the x-direction. A set of 3-D accelerometers (Analog Devices, ADXL327, sensitivity 0.42 V/g) embedded in the granular medium records the vibrations. Data acquisition is performed using a Matlab-controlled digitiser card (National Instrument USB-6010, 250 kHz, 16 channels). The accelerometers are placed every 4.5 cm from $x = 9.5$ cm to $x = 27.5$ cm, at $y_0 = 9$ cm and $z = 0$ (depicted by gray squares in Fig. 2. Placing them at a horizontal distance from the impact zone y_0 prevents damage to the devices by the penetrating bullet. We also consider that the aperture did not influence the confining pressure at the depth where wave propagation was analyzed ($y > 10$ cm).

The wave speed is measured with a confining pressure ranging from $p_{min} = 7.6$ kPa to $p_{max} = 164 \pm 5$ kPa. p_{min} corresponds to the weight of the material distributed over the floor area of the box. Subsequently, we incrementally increase the confining pressure by slowly pumping the hydraulic jack. The maximum pressure is manually set to be above p_{max}. For the vibration source, the increase is continuous, while measurements during impacts are conducted in 20 kPa increments. The duration of the rise, ranging from 10 to 150 s, does not significantly affect the wave speed.

Table 2
Characteristics of the shooting devices and their projectiles. Guns: spring-piston air rifle, CO_2 pistol, and crossbow. For each gun, the characteristics of the corresponding projectile are listed, including diameter, mass, and material. The velocity was measured using a bullet chronograph (PosChrono DLX), which detects the projectile's speed by measuring the time it takes to pass between two optical sensors. The uncertainty was computed as the standard deviation over 35 shots. The energy column represents the kinetic energy $e = m_p v^2/2$, with a 1% uncertainty omitted in the table.

Device	Projectile properties				
Gun	Diameter (mm)	Mass m_p (g)	Material	Velocity v (m/s)	Energy e (kJ)
Riffle	5.5	1.0	Lead	239 ± 4	28.6
Pistol	4.5	0.35	Steel	171 ± 3	5.1
Crossbow	6	0.9	Copper	66 ± 2	1.9

3. Seismic wave propagation during loading-unloading cycles

In this section, we provide an overview of the experimental characterization of seismic waves propagating in three different media and for four distinct sources. A numerical simulation is used to replicate the experimental configuration, ensuring that the apparent velocity aligns with the compressional wave velocity of the granular media for each confining pressure step. Finally, we analyze the dependency of the wave speed on the confining pressure.

3.1. Experimental characterization of the seismic wave propagation

Granular media seismic waves are characterized by recording material acceleration at a 15-kHz sampling frequency (Fig. 3. The x-component, which represents the primary wave propagating along the x-axis, is captured. The y-component has an amplitude approximately one-tenth that of the x-component and is therefore not shown. However, the relative phase between the x- and y-components is consistent with the propagation of the P-wave. The observable range for direct wave propagation spans 0 to 3 ms. The presentation of the peak amplitudes in relation to the propagation distance is depicted in Fig. 4. It should be noted that accelerometer saturates beyond 6 $\mathrm{m/s^2}$. Measurements of peak acceleration at different confining pressures did not yield significant variations. This lack of variation could be attributed to the uncertainty of measurement and the inherent scatter in the results of repeated experiments. Consequently, the peak amplitudes were averaged across different confining pressures to obtain reliable data. The exponential reduction of amplitude serves as a metric for quantifying attenuation, as elaborated in Section 3.2.

The time signals depicted in Fig. 3 show a characteristic waveform spread attributed to attenuation, which influences the frequency content. The central frequency of the waves was determined by analyzing the frequency content of the acceleration signals recorded by the accelerometers located at various distances from the source. Although the central frequency varies with distance from the source, this variation remains consistent across all sources and confining pressures. Therefore, we chose to represent it as an average across all sensors for each experiment. Fig. 5a presents example spectra of acceleration signals generated by the crossbow at different confining pressures. The peak frequency is defined as the maximum of the spectrum within the range of 0 to 1000 Hz.

Waves generated by impacts exhibit a central frequency ranging between 200 Hz and 500 Hz; see Fig. 5b. This frequency increase aligns with the well-established principle in spectral analysis of vibrations,

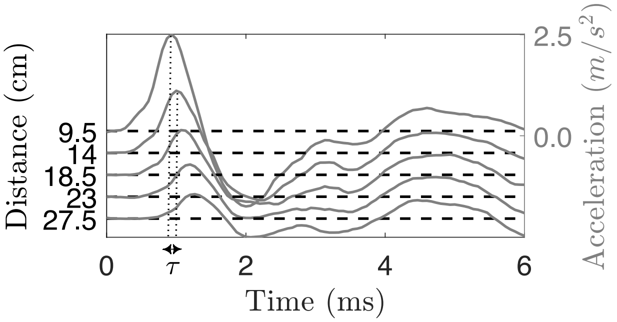

Fig. 3. The x-component accelerations signals along the measured at different position are represented as a function of time in a seismogram. The seismic wave was generated by the impact of a crossbow projectile in glass beads for a confining pressure of 20 kPa. The peak acceleration for $x = 9.5$ cm is 2.5 $\mathrm{m/s^2}$. The time delay τ between two signals is computed via cross-correlation to estimate the wave speed.

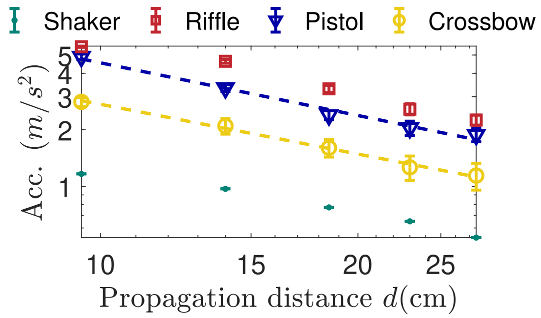

Fig. 4. The average peak acceleration amplitude, computed across all pressures, is plotted against propagation distance for various sources (as shown by the color-coded legend). The dashed lines represent the numerical simulation an attenuation coefficient of $\alpha = (1.8 \pm 0.2)$ Np/m (refer to Section 3.2). Uncertainty is determined through the propagation of residual errors.

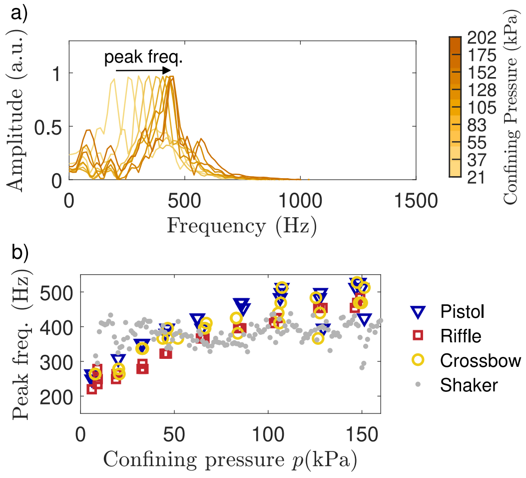

Fig. 5. (a) Normalized amplitude spectra of the acceleration signals from crossbow impacts for different confining pressures, represented by a color gradient indicating increasing pressure in the colorbar. It highlights the shift in peak frequency with increasing pressure. b) The peak frequencies from the acceleration signals for both, impacts (as shown in a) for crossbow, and shaker excitations, plotted as a function of confining pressure for glass beads. Various symbols represent experiments conducted with different projectiles and the shaker.

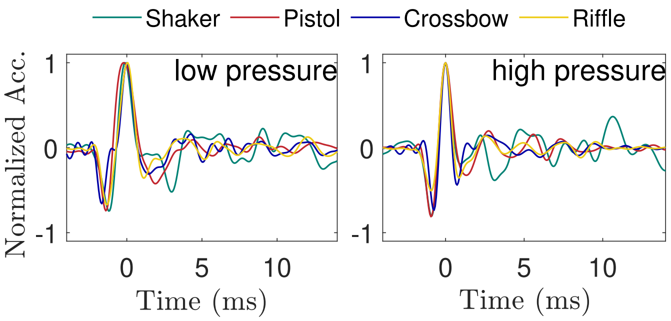

Fig. 6. Time signals from the first accelerometer for different impact sources are shown for low (≈50 kPa, left) and high (≈160 kPa, right) confining pressures. The signals exhibit a narrowing effect as pressure increases, while no significant differences are observed between the different impact sources.

where the frequency content depends on the hardness of the impacting tool (Mali and Singru, 2018). A harder impact tool generates higher frequencies when hitting a given material. Invoking spatial reciprocity, this means that a harder-impacted material also results in higher frequencies. In our experiments, the increase in central frequency with confining pressure is consistent with the increase in elasticity of the granular medium. Unlike the impact source, the shaker imposes a controlled waveform, where the central frequency is dictated by its mechanical response to a Heaviside excitation, preventing the frequency shift observed in impact-generated waves. However, the variation in projectile energy (see Table 2) does not significantly alter the peak frequency.

To provide a direct comparison of the different sources, Fig. 6 presents the waveforms recorded at the sensor position $x = 14$ cm for each source type, both at low (50 kPa) and high (160 kPa) confining pressures. No significant differences are observed between the signals from different impact sources as seen in Fig. 6, both under low and high confining pressures. The wave speed ($V = \delta x/\tau$) was determined by evaluating the time lag (τ) between two sensor signals separated by δx. An estimation of the time lag τ is shown in Fig. 3, where the position of the maximum of the cross-correlation is accurately determined using quadratic interpolation, a well-established robust method (Cespedes et al., 1995). Within this 14–26 cm depth range, all possible pairs of accelerometers are used to experimentally estimate the wave speed using the cross-correlation method depicted in Fig. 3 The correlation coefficients exhibit a minimum value of 0.80, with an average of 0.89. The wave speed, presented as a function of the confining pressure in Fig. 7a, is averaged over five trials for each impact attempt at constant pressure. The standard deviation of these five measurements is taken as the uncertainty represented by the error bars. This uncertainty accounts for the general variability in wave speed measurements, incorporating contributions from factors such as impactor speed and angle, travel-time measurement errors, distance measurement inaccuracies, and signal noise. It ranges from 50 m/s at low pressure to 100 m/s at maximum pressure.

A distinct increase is evident in Fig. 7a, where the wave speed rises from 130 m/s at p_{min} to 720 m/s at p_{max} when measured with the shaker as the source. With impacted sources, this elevation is similar and reaches 960 ± 196 m/s. Despite the wide range in the kinetic energy of the projectiles (see Table 2), the wave speed measurements do not show a clear dependency on it. There is no measurable difference between compression and relaxation, except at low pressure ($p < 50$ kPa). This suggests that within this frequency range, the granular medium does not exhibit hysteresis. Another notable observation, together with Fig. 6, is the striking similarity in the dependence on confining pressure between Shaker-born waves and impact-born waves (see Fig. 7a). This

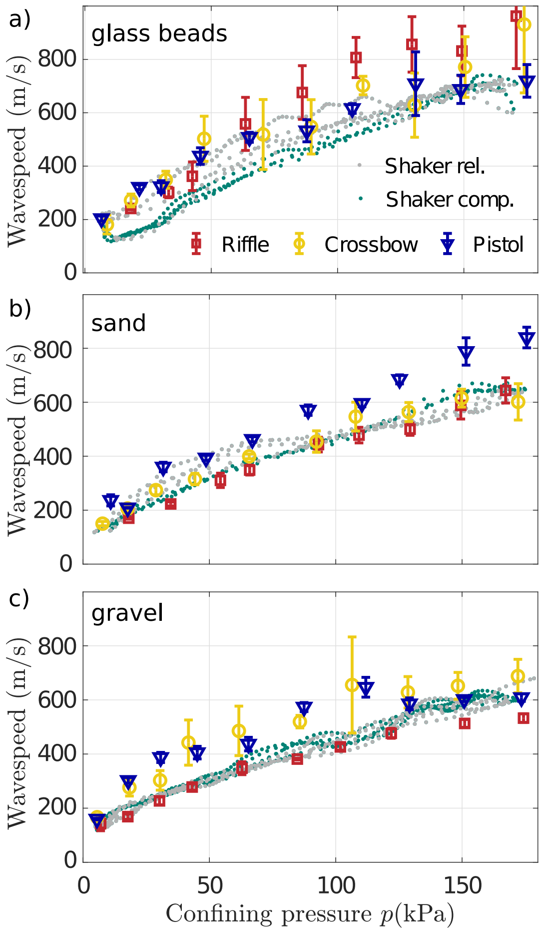

Fig. 7. Wave speed as a function of the confining pressure in (a) glass beads, (b) sand, and (c) gravel. Different symbols represent experiments with different projectiles, guns, and the shaker. For the shaker, we show data during several runs of the compression (gray dots) and relaxation (green dots) phases. For the different impacts, we compute the mean and standard deviation of the wave speed in each pressure step.

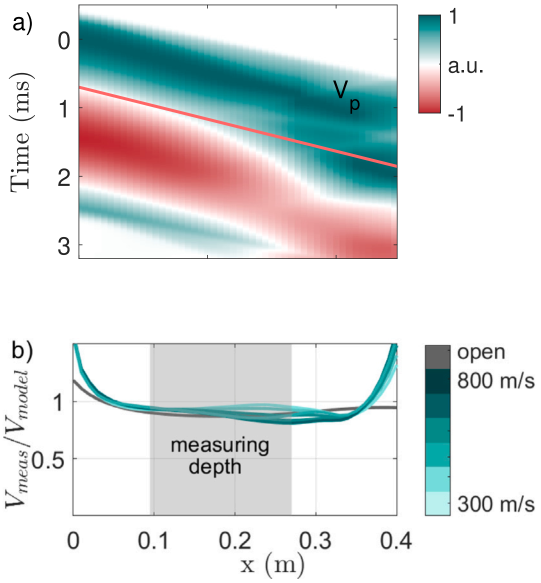

Fig. 8. (a) Numerical simulation of an elastic wave propagating in a closed 3D media as a function of time and along the $\vec{x}$-axis under the source ($y = 0$ cm). The color scale indicates the wave amplitude normalized at each depth (arbitrary units). The red line indicates the propagation time at the P-wave speed model $V_{model} = 300$ m/s. (b) Apparent wave speeds estimated by correlation are normalized by the model P-wave speed ranging from 200 to 800 m/s as indicated by the color legend. The wave speed in open media is represented in dark gray for comparison ($\lambda = 0.5$ m). The measuring gray zone indicates the accelerometer position in the experiment.

implies that the effects of impacts, such as fragmentation, grain reorganization, and nonlinear propagation, diminish before the wave reaches the measurement region.

Figs. 5 and 7 reveal that the wavelengths $\lambda = V/f$ range from 0.5 m to almost 2 m. These values are three orders of magnitude larger than the grains ($d \sim 0.25$ mm). In this regime $\lambda/d \gg 10$, coherent waves propagate in equivalent homogeneous material (Le Gonidec and Gibert, 2007). There is no multiple scattering, and the attenuation is not related to the diffusive propagation regime (Langlois and Jia, 2015). Wavelengths of impacted waves in a 300-m fractured asteroid have been estimated to be in the range of 1 to 100 m (Richardson et al., 2005). This suggests that a similar non-diffusive propagation regime may occur at real asteroid scales. In the following analysis, we retain the assumption of an equivalent homogeneous material and investigate the influence of the experimental domain's finite size relative to the wavelength.

3.2. Validation of wave speed measurements in sub-wavelength regions

This section aims to demonstrate that the wave speeds measured experimentally in Fig. 7 represent a fundamental property of the propagation medium: the P-wave velocity. Wavelength analysis confirms that the wavefield is sampled in a sub-wavelength regime, with a sampling interval (4.5 cm) significantly smaller than the wavelength. Dense array measurements with sub-wavelength sensor spacing have proven effective for extracting wave information in geophysics (Aki, 1967; Bonnefoy-Claudet et al., 2022; Hillers et al., 2016; Roux et al., 2016). However, boundary conditions can introduce measurement biases, as noted by Alshameri (2023). We therefore systematically assess diffraction effects arising from three key factors: (1) source dimensions and proximity, (2) boundary conditions, and (3) P-wave/S-wave interactions. We conduct a numerical investigation of 3D viscoelastic wave propagation within the experimental configuration to assess potential biases and validate our measurements. By accounting for geometrical spreading, attenuation, wave interference in a closed medium, source spatial extension, and the limited measurement region relative to the wavelength, we ensure confidence in the reliability of our measurements.

Given that the grain size is a thousand times smaller than the wavelength as mentioned in Section 3.1, assuming homogeneity regarding wave propagation is justified. Accordingly, the wave propagation simulation is carried out in a linear, homogeneous viscoelastic medium for each specific P-wave speed. We assume linearity in wave propagation, while nonlinearity is attributed to quasistatic perturbations, aligning with a common assumption in the nonlinear characterization of rocks (Guyer and Johnson, 2009). Each confining pressure step represents a distinct medium with its own P-wave speed, corresponding to a different confining pressure. The nonlinear nature of the granular media is considered only when there are changes in confining pressure, not during actual propagation events.

Numerical simulations were performed using the *k-wave* Matlab toolbox employing a pseudospectral method (Treeby et al., 2018; Treeby and Cox, 2010; Treeby et al., 2012). The homogeneous density is $\rho = 1650$ kg/m^3. The density increase $\Delta_\rho/\rho = \epsilon \sim 3\%$ at the maximum confining pressure is neglected. In this context of compression and wave propagation along the compression direction, the key parameter is the P-wave speed.

However, since an S-wave speed value is required, we adopt a P- to S-wave ratio of $V_p/V_s = \sqrt{3}$ (Stein and Wysession, 2009), which corresponds to a frictionless EMT model. The difference with a friction

EMT model ($V_p/V_s = \sqrt{2}$) is not significant. The P-wave speed is varied between 200 and 800 m/s.

The impact of the projectile is simulated by applying a force along the $\vec{x}$ -axis on an 8 cm diameter disc positioned in the $\vec{z}$-$\vec{y}$ plane, centred at the coordinate origin. The chosen source diameter approximates the size of the crater. The source is modeled as a time-dependent force with a single cycle sinusoidal motion at 400 Hz, chosen as the central frequency to simplify the analysis of wave speed and attenuation, rather than to replicate the exact waveform, as shown in Fig. 3. The sensors are located along the $\vec{x}$ axis at a distance of y_0 from the impact centre. The spatial grid step was set at 1 cm and the time step is 15 μs. A convergence test was conducted to ensure that the 1-cm grid step provides sufficient accuracy, while the time step was determined based on a Courant–Friedrichs–Lewy (CFL) number of 0.3 (see k-wave user manual (2016)).

Viscoelastic propagation in a 3D homogeneous medium is managed using a large Perfectly Matched Layer (20 points). We introduce an attenuation coefficient α into the k-wave solver as described by Firouzi et al. (2012). The impedance contrast between the granular media and acrylic ranges from 0.2 to 0.7, and can be neglected compared to the impedance contrast 10^2 between air and the granular media. The surrounding medium is modeled with both density and wave speed ten times smaller than the propagating medium, achieving a 10^2 impedance contrast while preventing numerical instabilities.

The attenuation coefficient is quantified by minimizing the difference between the numerical peak acceleration A_n and the experimental peak acceleration A_e depicted in Fig. 4, the attenuation coefficient is estimated to be $\alpha = (1.8 \pm 0.2)$ Np/m. The corresponding amplitudes are represented in dashed lines in Fig. 4. In particular, this attenuation value is four orders of magnitude higher than in rocks (Liu et al., 2020) and one order of magnitude higher than in dry sand at 500 Hz (Koerner et al., 1976). However, the latter comparison is based on a single study from 1976, and differences in experimental conditions, particularly the measurement method and potential moisture content, could explain this discrepancy.

The x-component of the particle velocity as a function of time and depth is illustrated in Fig. 8a, considering a P-wave speed of $V_p = 300$ m/s. To enhance visualization, the waveform is normalized by $A(x)$, the maximum amplitude at each depth. Reflection on the wall ($x = 50$ cm) creates interference between x-negative and x-positive propagation directions, as observed in Fig. 8a at $x \sim 0.35$ m. The attenuation minimizes bias in the wave-speed estimation in this region.

Fig. 8b depicts the apparent wave speed as a function of depth, estimated by cross-correlation, for various modeled wave speeds, aligned with the measurements in Fig. 7a, including an open media model. The open media model displays two notable features: (1) wave speeds exceeding V_p near the source due to the extended source size, and (2) apparent wave speeds reduced to 87% of V_p from sub-wavelength ($x < \lambda$, where $\lambda = 50$ cm) S-wave interactions. These effects persist in the closed media case, with the near-source effect being amplified by proximity to the interface. The S-wave interaction varies with wavelength, which spans 0.5–2 m.

The estimated wave speed from the numerical simulations is normalized by the P-wave speed value. The gray zone indicates the positions of the accelerometers used in the wave speed estimation. The average wave speed ranges from 99% to 86% in the P-wave speed model. Furthermore, there is no discernible trend between the absolute P-wave speed and the disparity between the modeled and estimated wave speeds. We can confidently conclude that the actual P-wave speed is measured in the experimental setup with an error of less than 14% ($V \approx V_p$), despite the finite size of the media. Consequently, the experiment provides relevant insights into wave propagation in an asteroid-like granular medium, particularly in the bulk. However, we acknowledge that differences in material properties, particle characteristics, and confining pressure limit a direct one-to-one scaling to real asteroids.

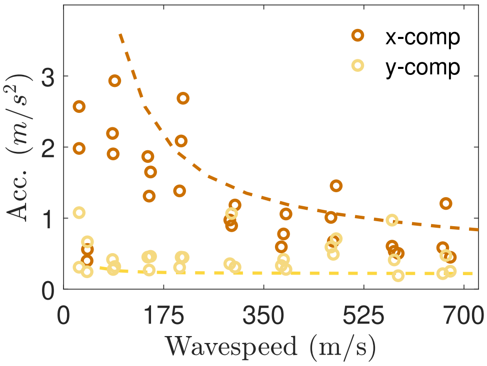

Fig. 9. Maximum acceleration peak as a function of the measured wave speed for crossbow signals. The x-component of the maximum acceleration is shown in brown, and the y-component in orange. The dashed lines represent acceleration peaks estimated from the numerical simulation as a function of the P-wave speed.

Finally we can compare the x-component and the y-component of the acceleration in Fig. 9 as a function of the measured wave speed. The projectile and the shaker creates a force along the x-direction and the main component of the acceleration is along the same direction. This signifies that the observed field corresponds to P-wave as mentioned in Section 3.1. To verify this, the numerical simulations were performed for the same wave speed range according to the measurements represented in Fig. 7a. The same amplitude (23 m/s^2) is set for each wave-speed (or pressure) simulation. Numerical simulations show a similar trend for both components, which is explained only by the wavelength growth and the relative P- to S-wave contribution at this particular spot. The simulation outputs separately compressive and shear strain. This confirms that the dominant x-component corresponds to compressive strain, providing unambiguous evidence that the observed wave is a P-wave.

In summary, this numerical study demonstrates that the P-wave speed of the granular medium can be accurately estimated within the experimental configuration, despite potential biases. By accounting for near-field effects, sub-wavelength measurements, and boundary influences, the simulation confirms that the measured wave speed corresponds to a fundamental property of the medium. This validation establishes a reliable link between the measured wave speed and the elastic modulus of the granular medium, considering confining pressure as a variable. The subsequent section will further analyze the dependency of elasticity on confining pressure.

4. On the dependence of the elasticity on the confining pressure

In this section, we examine the dependency of the wave speed on the confining pressure. Our analysis is based on the hypothesis that confined granular media behave similarly to rock, since rock itself is a cemented granular material. First, we present an elasticity model that fits the experimental measurements. Then, we apply this model to estimate the wave speed in an asteroid and perform numerical simulations of wave propagation.

4.1. Elasticity model

The expression for the EMT P-wave speed, as presented in Makse et al. (1999), is given by:

$$V_{\text{emt}} = \frac{3}{\sqrt{10\rho}}\left(\frac{\phi k_n C}{6\pi}\right)^{1/3} p^{1/6}, \qquad (1)$$

Here, C represents the coordination number or the average number of contacts per particle. The p^n dependency of the wave speed (P- or S-wave) may vary when considering other effects, such as contact

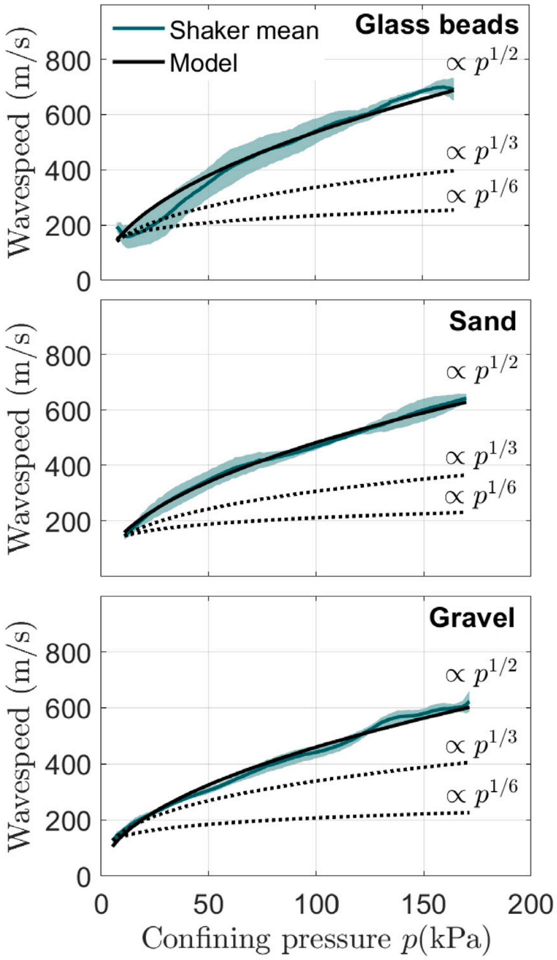

Fig. 10. The wave speed as a function of the confining pressure for (a) glass beads, (b) sand, and (c) gravel. The shaded areas correspond to the standard deviation of the shaker data. The average velocity induced by the shaker, depicted by a thick aquamarine line, varies with the confining pressure. Fig. 7 captures the dispersion of the data. Additionally, trend lines with dependencies of $p^{1/6}$, $p^{1/3}$, and $p^{1/2}$ corresponding to EMT models are represented by dashed lines, along with the mesoscopic model, respectively.

asphericity (Goddard, 1990) or the change of the coordination number ($n = 1/4$ for both assumptions) (Goddard, 1990; Agnolin and Roux, 2007). The higher experimental estimates of the exponent are in soils $n = 1/3$ (Wichtmann and Triantafyllidis, 2004) and $n = 1/2.5$ (Imhof and Santamarina, 2012). In Fig. 10, the best fit is clearly for $n = 1/2$. In addition, curves for $n = 1/2, 1/3, 1/6$ are shown to highlight the differences.

Rocks are aggregates of minerals and can be considered as cemented granular media. Elasticity in rocks exhibits mesoscopic nonlinearity, rooted in considerations of nonlinear elastic energy. This energy is expressed as a function of three invariants derived from the Lagrangian strain. The elasticity of a solid, when considering a third order of energy, can be encapsulated by the equation $M_{\text{solid}} = M_o\left(1 + \beta_c \epsilon\right)$, where M_0 denotes the elasticity in the absence of external perturbations (Guyer and Johnson, 2009), and β_c signifies the parameter of second order nonlinearity. This parameter is defined with respect to a positive compressive strain ϵ. In contrast to rocks, granular media lack inherent elasticity without external force. Consequently, the elasticity is zero without strain, resembling fluid behavior. In this context, we propose a mesoscopic expression of non-linearity for granular media to explain our observations. This expression, adapted from Guyer and Johnson (2009), is given by $M = M_0 \beta_c \epsilon$. Introducing a non-hysteretic linear pressure-strain relationship, $\epsilon = p/M_0$ yields a simple dependence of M on pressure:

$$M = \beta_c p. \tag{2}$$

The associated wave speed $V_{meso}^2 = M/\rho$ is deduced as follows:

$$V_{meso} = \left(\frac{\beta_c}{\rho} p\right)^{1/2}. \tag{3}$$

The second-order nonlinear parameters β_c were computed by minimizing the sum of the squared differences between the model and the data. A reasonable agreement is observed between the experimental data in Fig. 10 and the wave speed calculated from Eq. (3), with $\beta_c = (4.7 \pm 0.1) \times 10^3$, $\beta_c = (3.5 \pm 0.1) \times 10^3$ and $\beta_c = (3.9 \pm 0.1) \times 10^3$ in glass beads, sand, and gravel, respectively. Uncertainty is determined through the propagation of residual errors.

This estimation of nonlinearity demonstrates a comparable order of magnitude as measurements in dense granular media through nonlinear harmonic generation with ultrasound (Brunet et al., 2008), where β_c ranges from 0.5×10^3 to 1.5×10^3. For consolidated granular materials, the β_c parameter is found to be an order of magnitude smaller. For example, in concrete, it is on the order of $\sim 100 - 200$ (Spalvier et al., 2020), while in rocks, it varies between 0.5 and 2×10^3 (Gallot et al., 2015; D Angelo et al., 2008).

The results in sand and gravel indicate that nonlinearity is not sensitive to grain size. The nonlinearity is slightly higher in glass beads than in natural materials. This may be explained by the grain's angularities or polydispersity. In conclusion, the responses of these media exhibit similar trends, suggesting a consistent mechanical behavior of confined granular materials under quasi-static loading for confining pressures below 200 kPa.

4.2. Numerical simulation of wave propagation in dimorphos

According to Eq. (3), the wave speed in a granular media is only related to the pressure and two mechanical parameters: density and mesoscopic nonlinearity. This result has been established for high pressure compared to the microgravity in small asteroids. The question of the pressure distribution in an asteroid is still a matter of debate. This discussion is beyond the scope of this work, and we choose the simplest model of hydrostatic equilibrium where the pressure only depends on the depth d from the surface of the asteroid as $p = \frac{2}{3}\pi\rho^2 d^2$.[1] Together with Eq. (3), the wave speed in a spherical asteroid can be expressed as:

$$V_{ast} = d\left(\frac{2}{3}\pi\beta_c\rho\right)^{1/2}. \tag{4}$$

The Dimorphos geometry has been widely described in Daly et al. (2024). We choose to simulate wave propagation in a 2D circular medium with diameter $R = 171.5$ m. This diameter is calculated as the average of the extents of the ellipse axis $A = 173$ m and $B = 170$ m, neglecting the $A/B = 1.02$ ellipsoidal elongation. The density is considered homogeneous with $\rho = 2761$ kg/m^3 (Daly et al., 2024). The nonlinear parameter is chosen as the average of the measured values in the different media $\beta_c = 4 \times 10^3$. The attenuation is neglected in this simulation to focus on arrival time and all amplitudes are arbitrary. With these assumptions, the wave speeds increase linearly from 0 on the surface to a maximum wave speed of 3.4 m/s in the centre of

---

[1] Interestingly, a much more complex model of rubble-pile asteroids as homogeneous isotropic self-gravitating rigid-plastic sphere based on the Drucker–Prager yield criterion gives the same expression with a factor of 4/15 instead of 2/3 (Sharma, 2013).

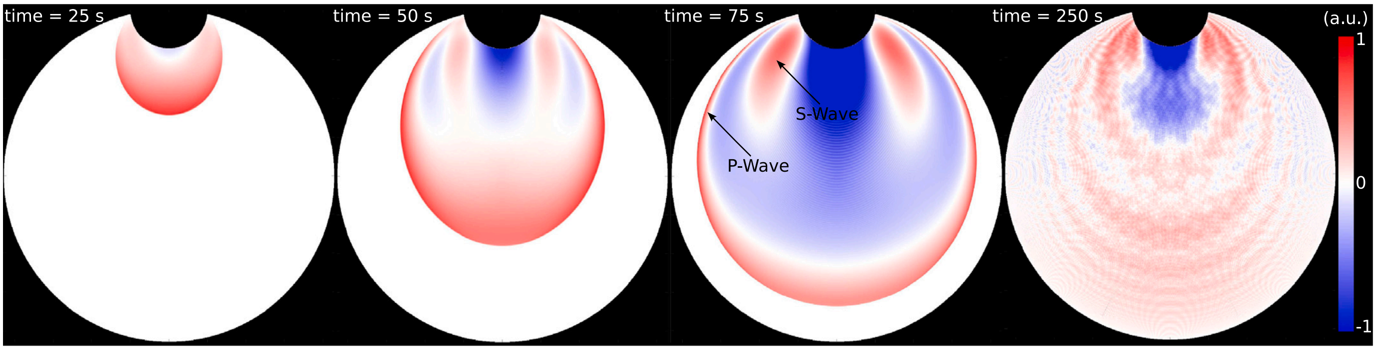

Fig. 11. Normalized acoustic pressure in a 2D-slice of a Dimorphos-like asteroid impacted from the top. The time after impact is indicated for each snapshots. The color scale on the right indicates the pressure in arbitrary unit (positive in red, negative in blue a.u.).

the asteroid. This simulation focusses on wave propagation under the assumption of solely reversible elastic deformation, pertinent to the period following the crater's formation, with material ejection not being considered.

Given that the projectile is approximately three orders of magnitude faster than the waves, the impact is modeled as an instantaneous and homogeneous volume injection throughout the entire crater region. The crater is considered a semisphere with a radius of 20 m, which falls within the lower range of the estimated size of the crater (Stickle et al., 2023). A fine grid point spacing of $d_x = 8$ cm was necessary to avoid spurious reflection along the circular asteroid border.

In the snapshots of the acoustic pressure field shown in Fig. 11, one can first observe the classic properties of wave propagation in solids, with an omnidirectional wavefront travelling at the speed of P-waves, followed by the separation of S-waves (time > 50 s, see arrows on Fig. 11) with a characteristic (bipolar) directionality. However, this wave directionality is modulated by the velocity gradient, creating an ovalization of the wavefront. At time $t = 75$ s, a decrease in wavelength is observed together with waves slowing as they approach the asteroid surface with a lower wave speed. According to Eq. (4), the wave speed decreases as it approaches the surface, theoretically tending toward zero. However, in reality, it never fully reaches zero, as the minimum depth is limited by the grain size. Consequently, the wave's travel time to emerge on the asteroid's surface is likely controlled by the grain size.

The observation of a wide-angle ejection cone ($138^{+2}_{-6}{}^\circ$ from Deshapriya et al. (2023) and $133 \pm 9°$ from Hirabayashi et al. (2025)) at over 170 s post-impact, with material being released from near Dimorphos' surface and at distances far from the impact site (54 ± 9) m or over 60° according to Hirabayashi et al. (2025), suggests that late-stage ejection occurred at low velocities. These findings align with the hypothesis that waves propagate slowly through the interior of the asteroid before resurfacing at distant locations. However, as our model does not explicitly compute particle velocities around the crater, we do not quantify whether these waves alone could induce ejection at escape velocity. Instead, we note that the timing and location of observed ejections are consistent with the expected arrival of internal waves, supporting the idea that seismic propagation may have contributed to the observed material lofting. However, this extrapolation does not account for predictions from numerical studies, such as Sánchez et al. (2022), which suggest a plateau in wave speed at low confining pressures, where the wave velocity becomes more dependent on the impactor velocity than on the confining pressure.

After the direct wave, the pressure field becomes progressively complex as a result of reverberations, wave conversions, and interference. The wave motions become more evenly distributed over time (as seen at $t = 250$ s in Fig. 11), with a reduction in maximum energy. This may contribute to later-stage low-velocity material ejections (Tancredi et al., 2023).

5. Concluding remarks

We conducted a comprehensive characterization of mechanical waves in confined granular media, examining frequencies up to approximately 500 Hz. At each confining pressure step, impacts and vibrations generated highly attenuated elastic waves that propagated consistently through the homogeneous granular media throughout the confining pressure range of 7–164 kPa. The absence of wave-diffusion-like processes was attributed to the significant difference in scale between the grain size and the wavelength, which spanned three orders of magnitude. The granular nature of the material was found to be relevant solely to understanding the influence of confining pressure on the equivalent homogeneous elasticity of the media. This conclusion was supported by the agreement between numerical simulation models and experimental observations on wave speed and amplitude. We also demonstrated that the waves generated by impacts and a shaker exhibited similar properties, appearing as P-waves with a dependency on the confining pressure following $p^{1/2}$. This dependency is consistent with a mesoscopic nonlinear model based on third-order nonlinear elastic energy.

The implications of this experimental characterization on low-pressure granular asteroids have also been studied. The mesoscopic nonlinearity estimation together with hydrostatic equilibrium hypothesis allows us to estimate the wave speed in an asteroid. Using the geometry and mass information of Dimorphos, we modeled wave propagation and found that the wave speed increases linearly with depth, reaching 3.4 m/s at the centre. These values were obtained by extrapolating our experimental data to much lower confining pressures than those directly tested. The alignment between the surface wave and the observed plume ejection suggests that wave propagation contributes to material ejection alongside direct impact. Near the surface, the waves slow down and the reverberated wave field may also play a role in later-stage ejections.

Although our study did not cover the gravity range under a few kPa, experiments in a low-gravity environment, like a space station or a drop tower, and/or realistic numerical simulations could extend the scope of our research. In this regard, our experiments revealed that the speed of impact-generated and shaker-born seismic body waves did not exhibit a strong dependence on the origin mechanism. This suggests that safer wave-generating methods, such as shakers, could be employed in low-gravity laboratory experiments instead of complex and risky impact devices. Finally, the findings presented in this study provide a valuable reference for testing numerical simulations using DEM and extending these simulations to a very low gravity regime, such as that found in asteroids hundreds of metres in size.

CRediT authorship contribution statement

Thomas Gallot: Writing – review & editing, Writing – original draft, Visualization, Validation, Supervision, Software, Resources, Project administration, Methodology, Investigation, Funding acquisition, Formal

analysis, Data curation, Conceptualization. **Camila Sedofeito:** Writing – review & editing, Writing – original draft, Visualization, Methodology, Investigation, Formal analysis, Data curation. **Alejandro Ginares:** Writing – review & editing, Investigation, Data curation. **Gonzalo Tancredi:** Writing – review & editing, Validation, Resources, Project administration, Methodology, Investigation, Formal analysis, Data curation, Conceptualization.

Declaration of competing interest

The authors declare that they have no known competing financial interests or personal relationships that could have appeared to influence the work reported in this paper.

Acknowledgments

The authors acknowledge financial support from projects FCE-1-2019-1-156451 and POS-NAC-2023-1-177572 of the Agencia Nacional de Investigación e Innovación ANII (Uruguay), the grant II-FVF-2019-145 of the “Fondo Vaz Ferreira” (D2C2-Ministerio de Educación *y* Cultura), the projects Grupos I+D Ciencias Planetarias C630-348 & C308-347 of the Comisión Sectorial de Investigación Científica (Udelar, Uruguay), and the Programa de las Ciencias Básicas (PEDECIBA-MEC, Uruguay).

Data availability

All our data are available upon reasonable request to the corresponding author. The k-wave package is available on http://www.k-wave.org/ under the GNU LGPL license.

References

Agnolin, I., Roux, J.-N., 2007. Internal states of model isotropic granular packings. III. Elastic properties. Phys. Rev. E 76 (6), 061304, https://doi.org/10.1103/PhysRevE.76.061304.

Aichele, J., Latour, S., Catheline, S., Roux, P., 2020. Imaging laboratory rupture nucleation at the source: A friction experiment using ultrafast ultrasound. In: EGU General Assembly Conference Abstracts. p. 22160. http://dx.doi.org/10.5194/egusphere-egu2020-22160.

Aki, K., 1967. Space and time spectra of stationary stochastic waves, with special reference to microtremors. Bull. Earthq. Res. Inst. 35, 415–456.

Alshameri, B., 2023. Investigate and analysis the efficiency of existing recommendations of near-field effect and boundary conditions on bender element technique. Pure Appl. Geophys. 180 (11), 3769–3785, https://doi.org/10.1007/s00024-023-03347-2.

Altshuler, E., Torres, H., González-Pita, A., Sánchez-Colina, G., Pérez-Penichet, C., Waitukaitis, S., Hidalgo, R., 2014. Settling into dry granular media in different gravities. Geophys. Res. Lett. 41 (9), 3032–3037, https://doi.org/10.1002/2014GL059229.

Badillo, E.J., 1974. Mecanica De Suelos I/Ground Mechanics I: Fundamentos de la Mecanica de Suelos/Fundamentals of Ground Mechanics, vol. 1, Editorial Limusa.

Ballouz, R.-L., Richardson, D.C., Michel, P., Schwartz, S.R., 2014. Rotation-dependent catastrophic disruption of gravitational aggregates. Astrophys. J. 789 (2), 158. http://dx.doi.org/10.1088/0004-637X/789/2/158.

Barnouin, O.S., Daly, R.T., Ernst, C.M., Gaskell, R.W., Nair, H., Agrusa, H., Chabot, N.L., Cheng, A.F., Dotto, E., Epifani, E.M., et al., 2024. An updated shape model of Dimorphos from DART data. Planet. Sci. J. 5 (24), http://dx.doi.org/10.3847/PSJ/ad09ba.

Betancourt, J.P.C., Delage, P., Caicedo, B., Lognonné, P., Banerdt, B., 2023. Wave velocities and Poisson ratio in a loose sandy martian regolith simulant under low stresses: 1. Laboratory investigation. J. Geophys. Res.: Planets 128 (11), e2023JE007988. http://dx.doi.org/10.1029/2023JE007988, URL: https://agupubs.onlinelibrary.wiley.com/doi/abs/10.1029/2023JE007988.

Bonnefoy-Claudet, S., Cornou, C., Garambois, S., 2022. Beyond SPAC: A review of seismic ambient noise methods. Surv. Geophys. 43, 133–176. http://dx.doi.org/10.1007/s10712-021-09674-5.

Brunet, T., Jia, X., Johnson, P.A., 2008. Transitional nonlinear elastic behaviour in dense granular media. Geophys. Res. Lett. 35 (19), https://doi.org/10.1029/2008GL035264.

Caicedo, B., Castillo Betancourt, J.P., Delage, P., Lognonné, P., Banerdt, B., 2023. Wave velocities and Poisson ratio in a loose sandy Martian regolith simulant under low stresses: 2. Theoretical analysis. J. Geophys. Res.: Planets 128 (11), e2023JE008008. http://dx.doi.org/10.1029/2023JE008008, URL: https://agupubs.onlinelibrary.wiley.com/doi/abs/10.1029/2023JE008008.

Cespedes, I., Huang, Y., Ophir, J., Spratt, S., 1995. Methods for estimation of subsample time delays of digitized echo signals. Ultrason. Imaging 17 (2), 142–171, https://doi.org/10.1103/PhysRevE.76.061304.

Cheng, A.F., 2004. Collisional evolution of the asteroid belt. Icarus 169 (2), 357–372. http://dx.doi.org/10.1016/j.icarus.2004.02.002.

Cheng, A., et al., 2023. Momentum transfer from the DART mission and the deflection of Dimorphos. Nature 616, 452–456, https://doi.org/10.1038/s41586-023-05878-z.

D Angelo, R., Winkler, K., Johnson, D., 2008. Three wave mixing test of hyperelasticity in highly nonlinear solids: Sedimentary rocks. J. Acoust. Soc. Am. 123 (2), 622–639, https://doi.org/10.1121/1.2821968.

Daly, R.T., Ernst, C.M., Barnouin, O.S., Gaskell, R.W., Nair, H., Agrusa, H., Chabot, N.L., Cheng, A.F., Dotto, E., Epifani, E.M., et al., 2024. An updated shape model of dimorphos from DART data. Planet. Sci. J. 5 (1), 24. http://dx.doi.org/10.3847/PSJ/ad0b07.

Daly, R., Ernst, C., Barnouin, O., et al., 2023. Successful kinetic impact into an asteroid for planetary defence. Nature 616, 443–447. http://dx.doi.org/10.1038/s41586-023-05810-5.

DellaGiustina, D., Ballouz, R.-L., Walsh, K., Marusiak, A., Bray, V., Bailey, S., 2024. Seismology of rubble-pile asteroids in binary systems. Mon. Not. R. Astron. Soc. 528 (4), 6568–6580, https://doi.org/10.1093/mnras/stae325.

DeMartini, J.V., Richardson, D.C., Barnouin, O.S., Schmerr, N.C., Plescia, J.B., Scheirich, P., Pravec, P., 2019. Using a discrete element method to investigate seismic response and spin change of 99942 Apophis during its 2029 tidal encounter with Earth. Icarus 328, 93–103, https://doi.org/10.1016/j.icarus.2019.03.015.

Deshapriya, J.D.P., Hasselmann, P.H., Gai, I., Hirabayashi, M., Dotto, E., Rossi, A., Zinzi, A., Corte, V.D., Bertini, I., Ieva, S., Epifani, E.M., Dall'Ora, M., Ivanovski, S., Perna, D., Farnham, T.L., Amoroso, M., Brucato, J.R., Capannolo, A., Caporali, S., Ceresoli, M., Chabot, N.L., Cheng, A., Cremonese, G., Daly, R.T., Fahnestock, E.G., Casajus, L.G., Gramigna, E., Impresario, G., Manghi, R.L., Lavagna, M., Li, J.-Y., Lombardo, M., Lucchetti, A., Modenini, D., Pajola, M., Palmer, E., Palumbo, P., Pirrotta, S., Poggiali, G., Rivkin, A.S., Sanchez, P., Tancredi, G., Tortora, P., Tusberti, F., Zannoni, M., Zanotti, G., 2023. Characterization of the DART impact ejecta plume on dimorphos from LICIACube observations. Planet. Sci. J. 4 (12), 231. http://dx.doi.org/10.3847/PSJ/ad09ba.

Dintwa, E., Tijskens, E., Ramon, H., 2008. On the accuracy of the Hertz model to describe the normal contact of soft elastic spheres. Granul. Matter 10 (3), 209–221, https://doi.org/10.1007/s10035-007-0078-7.

Duran, J., 2012. Sands, Powders, and Grains: an Introduction to the Physics of Granular Materials. Springer Science & Business Media.

Fahnestock, E.G., Cheng, A.F., Ivanovski, S., Michel, P., Raducan, S.D., Rossi, A., Abell, P.A., Chesley, S., Dotto, E., Ferrari, F., Kolokolova, L., Kramer, E., Li, J.-Y., Schwartz, S.R., Soldini, S., Tancredi, G., Campo Bagatin, A., Zhang, Y., 2022. Pre-encounter predictions of DART impact ejecta behavior and observability. Planet. Sci. J. 3 (9), 206. http://dx.doi.org/10.3847/PSJ/ac7fa1.

Firouzi, K., Cox, B., Treeby, B., Saffari, N., 2012. A first-order k-space model for elastic wave propagation in heterogeneous media. J. Acoust. Soc. Am. 132 (3), 1271–1283, https://doi.org/10.1121/1.4730897.

Fujiwara, A., Kawaguchi, J., Yeomans, D., Abe, M., Mukai, T., Okada, T., Saito, J., Yano, H., Yoshikawa, M., Scheeres, D., et al., 2006. The rubble-pile asteroid Itokawa as observed by Hayabusa. Science 312 (5778), 1330–1334. http://dx.doi.org/10.1126/science.1125841.

Gallot, T., Malcolm, A., Szabo, T.L., Brown, S., Burns, D., Fehler, M., 2015. Characterizing the nonlinear interaction of S-and P-waves in a rock sample. J. Appl. Phys. 117 (3), 034902, https://doi.org/10.1063/1.4905913.

Garcia, R.F., Murdoch, N., Mimoun, D., 2015. Micro-meteoroid seismic uplift and regolith concentration on kilometric scale asteroids. Icarus 253, 159–168, https://doi.org/10.1016/j.icarus.2015.02.014.

Goddard, J.D., 1990. Nonlinear elasticity and pressure-dependent wave speeds in granular media. Proc. R. Soc. Lond. Ser. A: Math. Phys. Sci. 430 (1878), 105–131, https://doi.org/10.1098/rspa.1990.0083.

Gómez, L.R., Turner, A.M., van Hecke, M., Vitelli, V., 2012. Shocks near jamming. Phys. Rev. Lett. 108 (5), 058001, https://doi.org/10.1103/PhysRevLett.108.058001.

Guyer, R.A., Johnson, P.A., 2009. Nonlinear Mesoscopic Elasticity: the Complex Behaviour of Rocks, Soil, Concrete. John Wiley & Sons.

Hestroffer, D., Sánchez, P., Staron, L., Bagatin, A.C., Eggl, S., Losert, W., Murdoch, N., Opsomer, E., Radjai, F., Richardson, D.C., et al., 2019. Small solar system bodies as granular media. Astron. Astrophys. Rev. 27 (1), 1–64, https://doi.org/10.1007/s00159-019-0117-5.

Hillers, G., Roux, P., Campillo, M., Ben-Zion, Y., 2016. Focal spot imaging based on zero lag cross-correlation amplitude fields: Application to dense array data at the San Jacinto fault zone. J. Geophys. Res.: Solid Earth 121 (11), 8048–8067, https://doi.org/10.1002/2016JB013014.

Hirabayashi, M., Raducan, S.D., Sunshine, J.M., Farnham, T.L., Deshapriya, J., Li, J.-Y., Tancredi, G., Chesley, S.R., Daly, R.T., Ernst, C.M., et al., 2025. Elliptical ejecta of asteroid Dimorphos is due to its surface curvature. Nat. Commun. 16 (1), 1602, https://doi.org/10.1038/s41467-025-56010-w.

Holsapple, K.A., 1993. The scaling of impact processes in planetary sciences. Annu. Rev. Earth Planet. Sci. 21 (1), 333–373.

Housen, K.R., Wilkening, L.L., 1982. The scaling of impact processes in planetary sciences. Annu. Rev. Earth Planet. Sci. 10 (1), 355–376.

Imhof, A.L., Santamarina, J.C., 2012. Seismic parameter evaluation of gravel and sand samples subjected to stress using general purpose piezocrystals. Geofísica Int. 51 (2), 109–119.

Jewitt, D., 2012. The active asteroids. Astron. J. 143 (3), 66. http://dx.doi.org/10.1088/0004-6256/143/3/66.

Jia, F., Cheng, H., Liu, S., Magnanimo, V., 2021. Elastic wave velocity and attenuation in granular material. In: EPJ Web of Conferences. EDP Sciences, p. 11001.

k-wave user manual, http://www.k-wave.org/manual/k-wave_user_manual_1.1.pdf.

Koerner, R.M., Curran, J.W., Mccabe, W.M., Lord Jr., A.E., 1976. Acoustic emission behavior of granular soils. J. Geotech. Eng. Div. 102 (7), 761–773, https://doi.org/10.1061/AJGEB6.0000297.

Langlois, V., Jia, X., 2015. Sound pulse broadening in stressed granular media. Phys. Rev. E 91 (2), 022205, https://doi.org/10.1103/PhysRevE.91.022205.

Latour, S., Schubnel, A., Nielsen, S., Madariaga, R., Vinciguerra, S., 2013. Characterization of nucleation during laboratory earthquakes. Geophys. Res. Lett. 40 (19), 5064–5069. http://dx.doi.org/10.1002/grl.50974.

Lauretta, D., DellaGiustina, D., Bennett, C., Golish, D., Becker, K., Balram-Knutson, S., Barnouin, O., Becker, T., Bottke, W., Boynton, W., et al., 2019. The unexpected surface of asteroid (101955) Bennu. Nature 568 (7750), 55–60, https://doi.org/10.1038/s41586-019-1033-6.

Le Gonidec, Y., Gibert, D., 2007. Multiscale analysis of waves reflected by granular media: Acoustic experiments on glass beads and effective medium theories. J. Geophys. Res.: Solid Earth 112 (B5), https://doi.org/10.1029/2006JB004518.

Li, J., Hirabayashi, M., Farnham, T., et al., 2023. Ejecta from the DART-produced active asteroid Dimorphos. Nature 616, 452–456. http://dx.doi.org/10.1038/s41586-023-05811-4.

Liu, X., Han, M., Li, X., Cui, J., Liu, Z., 2020. Elastic wave attenuation characteristics and relevance for rock microstructures. J. Min. Sci. 56 (2), 216–225, https://doi.org/10.1134/S1062739120026674.

Makse, H.A., Gland, N., Johnson, D.L., Schwartz, L.M., 1999. Why effective medium theory fails in granular materials. Phys. Rev. Lett. 83 (24), 5070, https://doi.org/10.1103/PhysRevLett.83.5070.

Mali, K.D., Singru, P.M., 2018. Study on the effect of the impact location and the type of hammer tip on the frequency response function (FRF) in experimental modal analysis of rectangular plates. In: Materials Science and Engineering Conference Series. 012102. http://dx.doi.org/10.1088/1757-899X/330/1/012102.

Martínez, F., Urrea, M.P., Gonzalez, C.M., Varas, G., 2021. Extending the Boussinesq model for impacts in granular media. Granul. Matter 23 (1), 1–6, https://doi.org/10.1007/s10035-020-01065-3.

Michel, P., Küppers, M., Bagatin, A.C., et al., 2022. The ESA Hera mission: Detailed characterization of the DART impact outcome and of the binary asteroid (65803) Didymos. Planet. Sci. J. 3 (7), 160. http://dx.doi.org/10.3847/PSJ/ac6f52.

Moreno, F., Bagatin, A.C., Tancredi, G., Li, J.-Y., Rossi, A., Ferrari, F., Hirabayashi, M., Fahnestock, E., Maury, A., Sandness, R., et al., 2023. Characterization of the ejecta from the NASA/DART impact on dimorphos: Observations and Monte Carlo models. Planet. Sci. J. 4 (8), 138. http://dx.doi.org/10.3847/PSJ/ace827.

Murdoch, N., Hempel, S., Pou, L., Cadu, A., Garcia, R., Mimoun, D., Margerin, L., Karatekin, O., 2017. Probing the internal structure of the asteriod Didymoon with a passive seismic investigation. Planet. Space Sci. 144, 89–105, https://doi.org/10.1016/j.pss.2017.05.005.

Pajola, M., Hasselmann, P.H., Gai, I., Hirabayashi, M., Dotto, E., Rossi, A., Zinzi, A., Corte, V.D., Bertini, I., Ieva, S., et al., Characterization of the DART impact ejecta plume on Dimorphos from LICIACube observations.

Quillen, A.C., Zhao, Y., Chen, Y., Sánchez, P., Nelson, R.C., Schwartz, S.R., 2019. Impact excitation of a seismic pulse and vibrational normal modes on asteroid Bennu and associated slumping of regolith. Icarus 319, 312–333, https://doi.org/10.1016/j.icarus.2018.09.032.

Raducan, S., Jutzi, M., Cheng, A., Zhang, Y., Barnouin, O., Collins, G., Daly, R., Davison, T., Ernst, C., Farnham, T., et al., 2024. Physical properties of asteroid Dimorphos as derived from the DART impact. Nat. Astron. 8 (4), 445–455, https://doi.org/10.1038/s41550-024-02200-3.

Richardson, Jr., J.E., Melosh, H.J., Greenberg, R.J., O'Brien, D.P., 2005. The global effects of impact-induced seismic activity on fractured asteroid surface morphology. Icarus 179 (2), 325–349, https://doi.org/10.1016/j.icarus.2005.07.005.

Rivkin, A.S., Chabot, N.L., Stickle, A.M., Thomas, C.A., Richardson, D.C., Barnouin, O., Fahnestock, E.G., Ernst, C.M., Cheng, A.F., Chesley, S., Naidu, S., Statler, T.S., Barbee, B., Agrusa, H., Moskovitz, N., Terik Daly, R., Pravec, P., Scheirich, P., Dotto, E., Della Corte, V., Michel, P., Küppers, M., Atchison, J., Hirabayashi, M., 2021. The double asteroid redirection test (DART): Planetary defense investigations and requirements. Planet. Sci. J. 2 (5), 173. http://dx.doi.org/10.3847/PSJ/ac063e.

Roux, P., Moreau, L., Lecointre, A., Hillers, G., Campillo, M., Ben-Zion, Y., Zigone, D., Vernon, F., 2016. A methodological approach towards high-resolution surface wave imaging of the San Jacinto Fault Zone using ambient-noise recordings at a spatially dense array. Geophys. J. Int. 206 (2), 980–992, https://doi.org/10.1093/gji/ggw193.

Rubinstein, S., Cohen, G., Fineberg, J., 2007. Dynamics of precursors to frictional sliding. Phys. Rev. Lett. 98 (22), 226103, https://doi.org/10.1103/PhysRevLett.98.226103.

Sánchez, P., Scheeres, D.J., Quillen, A.C., 2022. Transmission of a seismic wave generated by impacts on granular asteroids. Planet. Sci. J. 3 (10), 245. http://dx.doi.org/10.3847/PSJ/ac960c.

Scheeres, D.J., Britt, D., Carry, B., Holsapple, K.A., 2015. Asteroid interiors and morphology. In: Asteroids IV. The University of Arizona Press, pp. 745–766. http://dx.doi.org/10.2458/azu_uapress_9780816532131-ch038.

Schöpfer, M.P., Abe, S., Childs, C., Walsh, J.J., 2009. The impact of porosity and crack density on the elasticity, strength and friction of cohesive granular materials: Insights from DEM modelling. Int. J. Rock Mech. Min. Sci. 46 (2), 250–261, https://doi.org/10.1016/j.ijrmms.2008.03.009.

Sharma, I., 2013. Structural stability of rubble-pile asteroids. Icarus 223 (1), 367–382. http://dx.doi.org/10.1016/j.icarus.2012.11.005.

Somfai, E., Roux, J.-N., Snoeijer, J.H., Van Hecke, M., Van Saarloos, W., 2005. Elastic wave propagation in confined granular systems. Phys. Rev. E 72 (2), 021301, https://doi.org/10.1103/PhysRevE.72.021301.

Spalvier, A., Domenech, L.D., Cetrangolo, G., Popovics, J.S., 2020. Torsional vibration technique for the acoustoelastic characterization of concrete. Mater. Struct. 53 (1), 1–17, https://doi.org/10.1617/s11527-020-1438-6.

Stein, S., Wysession, M., 2009. An Introduction to Seismology, Earthquakes, and Earth Structure. John Wiley & Sons.

Stickle, A.M., DeCoster, M.E., Burger, C., Caldwell, W.K., Graninger, D., Kumamoto, K.M., Luther, R., Ormö, J., Raducan, S., Rainey, E., Schäfer, C.M., Walker, J.D., Zhang, Y., Michel, P., Michael Owen, J., Barnouin, O., Cheng, A.F., Chocron, S., Collins, G.S., Davison, T.M., Dotto, E., Ferrari, F., Isabel Herreros, M., Ivanovski, S.L., Jutzi, M., Lucchetti, A., Martellato, E., Pajola, M., Plesko, C.S., Bruck Syal, M., Schwartz, S.R., Sunshine, J.M., Wünnemann, K., 2022. Effects of impact and target parameters on the results of a kinetic impactor: Predictions for the double asteroid redirection test (DART) mission. The Planet. Sci Journal. 3 (11), 248. http://dx.doi.org/10.3847/PSJ/ac91cc, https://dx.doi.org/10.3847/PSJ/ac91cc.

Stickle, A., Graninger, D., Group, D.I.M.W., et al., 2023. Impact simulations provide important constraints on Dimorphos's material properties and estimates of crater size from the DART impact. LPI Contrib. 2851, 2541.

Tancredi, G., 2015. The "Main-Belt Comets" are not comets, nor active asteroids; they are temporary shaken asteroids. IAU Gen. Assem. 29, 2255319.

Tancredi, G., Liu, P.-Y., Campo-Bagatin, A., Moreno, F., Domínguez, B., 2023. Lofting of low-speed ejecta produced in the DART experiment and production of a dust cloud. Mon. Not. R. Astron. Soc. 522 (2), 2403–2414. http://dx.doi.org/10.1093/mnras/stac3258, arXiv:2209.02805.

Tancredi, G., Maciel, A., Heredia, L., Richeri, P., Nesmachnow, S., 2012. Granular physics in low-gravity environments using discrete element method. Mon. Not. R. Astron. Soc. 420 (4), 3368–3380. http://dx.doi.org/10.1111/j.1365-2966.2011.20259.x.

Thomas, C., et al., 2023. The successful deflection of Dimorphos: Observations and implications. Nature 616, 448–451. http://dx.doi.org/10.3847/PSJ/ad4350.

Treeby, B.E., Budisky, J., Wise, E.S., Jaros, J., Cox, B., 2018. Rapid calculation of acoustic fields from arbitrary continuous-wave sources. J. Acoust. Soc. Am. 143 (1), 529–537, https://doi.org/10.1121/1.5021245.

Treeby, B.E., Cox, B.T., 2010. k-Wave: MATLAB toolbox for the simulation and reconstruction of photoacoustic wave fields. J. Biomed. Opt. 15 (2), 021314.

Treeby, B.E., Jaros, J., Rendell, A.P., Cox, B., 2012. Modeling nonlinear ultrasound propagation in heterogeneous media with power law absorption using ak-space pseudospectral method. J. Acoust. Soc. Am. 131 (6), 4324–4336, https://doi.org/10.1121/1.4712021.

Villalobos, C., Housset, M., Varas, G., 2022. Geometrical description of impact cratering under microgravity conditions. Granul. Matter 24 (2), 1–7, https://doi.org/10.1007/s10035-022-01221-x.

Walsh, K.J., 2018. Rubble pile asteroids. Annu. Rev. Astron. Astrophys. 56 (1), 593–624. http://dx.doi.org/10.1146/annurev-astro-081817-052013, arXiv:https://doi.org/10.1146/annurev-astro-081817-052013.

Walton, K., 1987. The effective elastic moduli of a random packing of spheres. J. Mech. Phys. Solids 35 (2), 213–226, https://doi.org/10.1016/0022-5096(87)90036-6.

Wang, Y., Mora, P., 2009. The ESYS_particle: a new 3-D discrete element model with single particle rotation. In: Advances in Geocomputing. Springer, pp. 183–228.

Watanabe, S., Hirabayashi, M., Hirata, N., Hirata, N., Noguchi, R., Shimaki, Y., Ikeda, H., Tatsumi, E., Yoshikawa, M., Kikuchi, S., et al., 2019. Hayabusa2 arrives at the carbonaceous asteroid 162173 Ryugu—A spinning top–shaped rubble pile. Science 364 (6437), 268–272. http://dx.doi.org/10.1126/science.aav8032.

Watters, T.R., Thomas, P.C., Robinson, M.S., 2011. Thrust faults and the near-surface strength of asteroid 433 Eros. Geophys. Res. Lett. 38 (2), https://doi.org/10.1029/2010GL045302.

Wichtmann, T., Triantafyllidis, T., 2004. Influence of a cyclic and dynamic loading history on dynamic properties of dry sand, part I: cyclic and dynamic torsional prestraining. Soil Dyn. Earthq. Eng. 24 (2), 127–147, https://doi.org/10.1016/j.soildyn.2003.10.004.

van den Wildenberg, S., van Loo, R., van Hecke, M., 2013. Shock waves in weakly compressed granular media. Phys. Rev. Lett. 111 (21), 218003, https://doi.org/10.1103/PhysRevLett.111.218003.

Yasui, M., Matsumoto, E., Arakawa, M., 2015. Experimental study on impact-induced seismic wave propagation through granular materials. Icarus 260, 320–331, https://doi.org/10.1016/j.icarus.2015.07.032.

Zhang, Y., Richardson, D.C., Barnouin, O.S., Michel, P., Schwartz, S.R., Ballouz, R.-L., 2018. Rotational failure of rubble-pile bodies: Influences of shear and cohesive strengths. Astrophys. J. 857 (1), 15. http://dx.doi.org/10.3847/1538-4357/aab5b2.